Chemical vapor deposition of iron, iron carbides, and iron nitride films from amidinate precursors

Vladislav V. Krisyuk, Alain Gleizes, Lyacine Aloui, Asiya E. Turgambaeva, Bartosz Sarapata, Nathalie Prud'Homme, François Senocq, Diane Samélor, Anna Zielinska-Lipiec, Dominique de Caro, et al.

Chemical Vapor Deposition of Iron, Iron Carbides, and Iron Nitride Films from Amidinate Precursors

Vladislav Krisyuk,[a,b] Alain N. Gleizes,[a] Lyacine Aloui,[a] Asiya Turgambaeva,[a,b] Bartosz Sarapata,[a,c] Nathalie Prud'Homme,[a] François Senocq,[a] Diane Samélor,[a] Anna Zielinska-Lipiec,[c] Dominique de Caro,[d] and Constantin Vahlas[a,z]

[a]*Centre Interuniversitaire de Recherche et d'Ingénierie des Matériaux, Ecole Nationale Supérieure d'Ingénieurs en Arts Chimiques et Technologiques, 31432 Toulouse Cedex 4, France*
[b]*Nikolaev Institute of Inorganic Chemistry, Siberian Branch of the Russian Academy of Science, Novosibirsk 630090, Russia*
[c]*Akademia Górniczno-Hutnicza University of Science and Technology, PL-30 059 Krakow, Poland*
[d]*Laboratoire de Chimie de Coordination, CNRS, 31077 Toulouse Cedex 4, France*

Iron bis(*N*,*N*′-diisopropylacetamidinate) $[Fe_2(\mu\text{-}^i\text{Pr-MeAMD})_2(\eta^2\text{-}^i\text{Pr-MeAMD})_2]$ and iron bis(*N*,*N*′-di-*tert*-butylacetamidinate) $[Fe(^t\text{Bu-MeAMD})_2]$ were used as precursors for the metallorganic chemical vapor deposition (MOCVD) of iron-containing compounds including pure iron, iron carbides, Fe_3C and Fe_4C, and iron nitrides Fe_4C. Their decomposition mechanism involves hydrogen migration followed by dissociation of the Fe–N bond and the release of free hydrogenated ligand (HL) and radicals. Surface intermediates are either released or decomposed on the surface providing Fe–N or Fe–C bonds. MOCVD experiments were run at 10 Torr, in the temperature ranges of 350–450°C with $Fe_2(\mu - {}^i\text{Pr-MeAMD})_2(\eta^2\text{-}^i\text{Pr-MeAMD})_2$ and 280–350°C with $Fe(^t\text{Bu-MeAMD})_2$. Films prepared from $Fe_2(\mu - {}^i\text{Pr-MeAMD})_2(\eta^2\text{-}^i\text{Pr-MeAMD})_2$ contain Fe, Fe_3C, and Fe_4C. Those prepared from $Fe(^t\text{Bu-MeAMD})_2$ contain Fe, Fe_3C, and also Fe_4C or Fe_4N, depending on the temperature and hydrogen to precursor ratio (H/P) in the input gas. The room-temperature coercive field of films processed from $Fe(^t\text{Bu-MeAMD})_2$ is 3 times higher than that of the high temperature processed Fe_4N films.

Iron-based metallic and ceramic films have a wide range of applications and there is an unfailing interest in developing and improving techniques for the processing of such films with innovative phase compositions. To mention but a few examples, the use of Fe films is foreseen in metallurgical applications;[1] films containing iron nitrides present not only mainly magnetic but also tribological and corrosion-resistant properties (Ref. 2 and references therein). Iron carbides have attracted attention due to their high hardness and melting point.[3] Although physical vapor deposition is widely used for these purposes, metallorganic chemical vapor deposition (MOCVD) is reputed to be a flexible and economically competitive method because it combines conformal coverage with high deposition rates and mild deposition conditions.[4] However, MOCVD of nitride and of metallic films has not been widely applied yet. Typical drawbacks are the contamination with carbon and the difficulty to control the composition and the microstructure of the films.

In the frame of an ongoing project, the authors are presently investigating the preparation of multimetallic films by co-depositing Fe and Al with the MOCVD technique. Such intermetallic systems can be used for the processing of coatings containing iron aluminides and more generally complex metallic alloys presenting unique combinations of properties.[5] To meet this objective, the selection of appropriate precursors is not simply limited to identifying metal complexes with similar volatilities and similar decomposition temperatures. Ideally, precursors for the chemical vapor deposition (CVD) of metals should be selected and treated so as to be cleanly decomposed (clean cleavage, stable ligands, ligand fragments, etc.) (see, for instance, Ref. 6). Co-depositing several metals requires considering the different chemistries of the metals. This is the case for a system containing aluminum and d-transition metals such as the Fe–Al couple. The highly electropositive character of aluminum excludes the presence of the most electronegative elements such as oxygen or fluorine in the precursors of both aluminum and the companion metal(s). Similarly, the affinity of iron to carbon leads to set Fe–C bonds containing precursors aside. Finally, ligand exchange reactions between the precursors must be avoided because they may induce dramatic volatility decrease. It is therefore necessary to test the selected precursors separately and then in pairs (see, for instance, Ref. 7). Consequently, one motivation of this work was to investigate an original process for the MOCVD of the Fe films.

Compared with other metals, few open scientific publications refer to the thermal MOCVD of pure iron films. $Fe(Cp)_2$,[1,8,9] $Fe(CO)_5$,[10-14] $Fe_2Cp_2(CO)_4$,[15] $Fe(COT)(CO)_3$,[16] and [(arene)(diene)Fe^0] [17] are known as iron precursors, but they do not meet the prerequisites of no oxygen and no Fe–C bond. $Fe[N(SiMe_3)_2]_3$ is worth testing, but the reported deposition temperature of 325°C [18] may be too high for the purpose of the co-deposition with Al. Fe(II) dihydride $H_2Fe[P(CH_3)_3]_4$ yielded pure α-Fe films between 230 and 280°C, but limited information was provided on the process itself and the obtained material.[19] Finally, Lim et al. showed that some transition-metal amidinates are volatile[20] and can be used as precursors for the atomic layer deposition (ALD) of transition-metal thin films.[21] Based on the latter papers, copper amidinates have been recently successfully tested for the deposition of copper.[22]

A parallel motivation of this work concerns the investigation of innovative MOCVD routes for the processing of iron nitrides. The motivation originates from the intrinsic magnetic properties of such materials, especially γ′-Fe_4N, combined with their high electrical conductivity and their chemically inert and mechanically hard surfaces (Ref. 23 and 24 and references therein). Line-of-sight techniques such as thermal evaporation, reactive sputtering, and laser ablation have been employed for the processing of iron nitride films (Ref. 25 and references therein). Alternatively, vapor-phase epitaxy involving iron trichloride ($FeCl_3$) and ammonia (NH_3) allowed the production of Fe_4N epitaxial layers, with the noticeable drawbacks of high processing temperature (600°C) and aggressive halide-based chemistry.[26] Few papers deal with the CVD of iron nitrides. Funakubo et al. reported on the formation of γ′-Fe_4N from biscyclopentadienyl iron and $NH_3/H_2/CO_2$ above 700°C.[27] Roberson et al. reported on the growth of Fe_3N from iron acetylacetonate and anhydrous NH_3 above 600°C.[2]

[z] E-mail: constantin.vahlas@ensiacet.fr

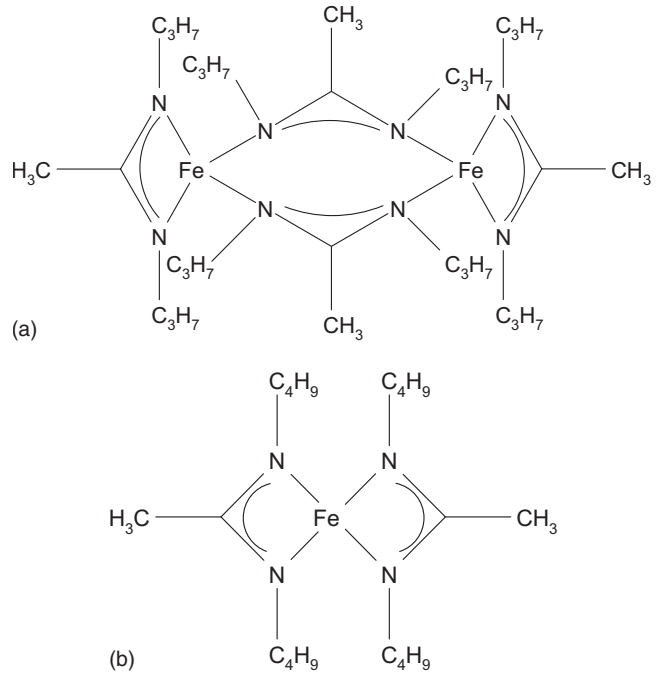

Figure 1. Developed formulas of (a) bis(*N*,*N*′-diisopropylacetamidinate)iron(II) (1), and of (b) bis(*N*,*N*′-di-*tert*-butylacetamidinate)iron(II) (2).

The present paper deals with the investigation of two iron amidinates as precursors for the MOCVD of Fe and Fe_4N: (1) dinuclear iron bis(*N*,*N*′-diisopropylacetamidinate) $[Fe_2(\mu\text{-}^{i}Pr\text{-}MeAMD)_2(\eta^2\text{-}^{i}Pr\text{-}MeAMD)_2]$ and (2) mononuclear iron bis(*N*,*N*′-di-*tert*-butylacetamidinate) $[Fe(^{t}Bu\text{-}MeAMD)_2]$.[20] These are nonoxygenated metallorganic complexes with ligand–metal bonding through Fe–N bonds (Fig. 1). Lim et al. showed that compound 2 could be used for the ALD of pure iron films.[21]

In what follows, information on the thermal behavior of the two precursors, investigated by in situ mass spectrometry, is first reported. The characteristics of the MOCVD processed films are then detailed, focusing on their elemental and phase composition, and morphology. Finally, the room-temperature magnetic properties of the films are reported and discussed.

Experimental

Precursor investigation.— Compounds 1 and 2 were synthesized by NanoMePS[e] by appropriately adapting the protocol of Lim et al.[20] They were used without further purification. Both compounds are extremely sensitive to air and light. Upon storage in a metallic glove box under a continuously purified argon flow, they slowly decomposed: The green powder of precursor 1 tarnished and the white powder of precursor 2 turned gray. The compounds must be kept in sealed ampoules at 4°C.

The gas-phase thermal decomposition of the precursors was studied by a technique which combines Knudsen effusion and mass spectrometric measurements of the gas-phase composition. The experimental details have been described elsewhere.[28] This investigation used a time of flight mass spectrometer directly fed by an input system that imitates a CVD reactor. 5 mg of the compound was sealed in a glass ampoule under inert gas and heated in the evaporator at 90 and 70°C for compounds 1 and 2, respectively. The evaporator temperature was kept constant, and the vapors were transported to the miniature CVD reactor through a heated pipeline. During the experiment, the reactor temperature was progressively raised from the temperature of evaporation to 400°C with a heating rate of 5°/min. The reaction mixture was sampled through the effusion hole (0.2 mm) from the reactor into the mass analyzer. Mass spectra were recorded at ionizing electron energies ca. 70 eV. The temperature dependence of the gas-phase composition was derived from the mass spectra.

Deposition.— The CVD experiments were conducted in two, stagnant-flow, vertical, tubular, cold wall reactors of similar configurations. Reactor A was composed of a glass tube containing an inductively heated, 20 mm diameter stainless steel susceptor. It was used for the initial screening of the two precursors. Reactor B was used for the processing of multimetallic coatings. It was composed of a stainless steel body and contained a resistively heated, 60 mm diameter stainless steel susceptor. A detailed description of the setup is provided in Ref. 29. A showerhead above the susceptor ensured homogeneous flow of the reactants on the surface of the substrates. The larger susceptor in reactor B allowed expanding the number and types of substrates processed in one run. The deposition from compound 1 was investigated in reactor A; the deposition from compound 2, which proved to be the more promising of the two precursors for the co-deposition of multimetallic films, was investigated in both reactors. The base pressure for both reactors was 1.0×10^{-6} Torr. Flow thermal and hydrodynamic characteristics were calculated so as to get laminar flows and similar operation conditions in either reactor (Ref. 29 and unpublished results).

Polycrystalline copper disks (10 mm in diameter, 1 mm thick) were used as substrates. The disappearance of copper color was optically tracked to access film growth onset. Before deposition, the substrates were polished with a diamond paste down to 5 μm. They were cleaned ultrasonically in acetone and anhydrous ethanol. Pure nitrogen (99.998%) and pure hydrogen (99.999%, Air Products) were fed through computer-driven mass flow controllers. The former was used both as carrier gas through the precursor container and as dilution gas. The deposition pressure was 10 Torr and the temperature of the substrates was in the range 150–450°C. The precursor container was maintained at 95 and at 85°C for precursors 1 and 2, respectively. Deposition was run for 1–4 h, depending on the operating conditions. Table I summarizes the flow rate conditions. The main difference in the processing conditions between reactors A and B is the ratio of the hydrogen to precursor concentration (hereafter referred to as H/P). Because the saturated vapor pressure vs temperature values are not actually available for these new compounds, it is not possible to quantify P and, subsequently, the H/P ratio. For this reason, it can only be mentioned that the H/P ratio is 3 to 4 times higher in reactor B than in A.

The deposited phases were identified by grazing incidence X-ray diffraction (GIXRD) with a Siefert 3000 diffractometer (Cu Kα radiation; grazing angle = 2–3°; 2θ step = 0.04°). Surface and cross section morphologies were investigated by a scanning electron mi-

[e] www.nanomeps.fr

Table I. Flow rate conditions for reactors A and B.

Flow rate (sccm)	Q(H_2)		Q(N_2, carrier)		Q(N_2, dilution)		Q(total)	
Precursor	1	2	1	2	1	2	1	2
Reactor A	50	80	20	20	30	0	100	100
Reactor B	—	285	—	20–40	—	20–0	—	325

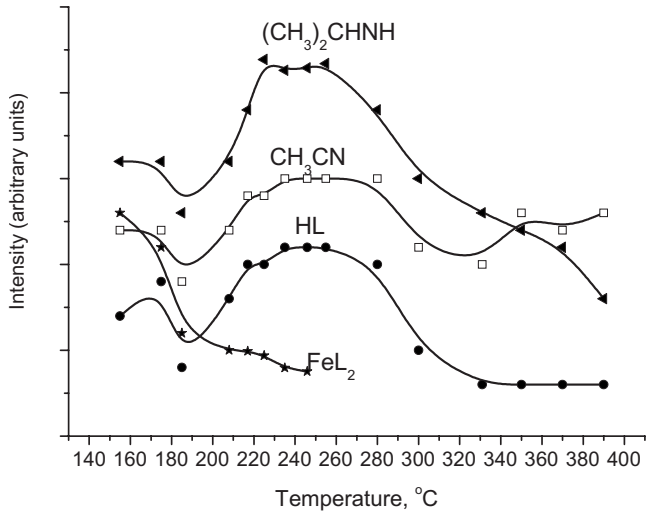

Figure 2. Temperature dependence of gas-phase composition upon decomposition of compound 1 [L = $(C_3H_7)NC(CH_3)N(C_3H_7)$]. The lines are guides for the eyes.

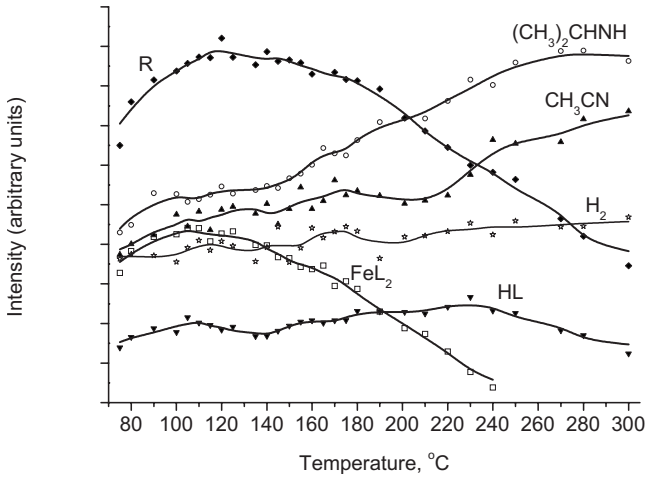

Figure 3. Temperature dependence of gas-phase composition upon decomposition of compound 2 in the presence of hydrogen [R = *tert*-butyl radical, C_4H_9; L = $RNC(CH_3)NR$]. The lines are guides for the eyes.

croscope (SEM) with a LEO 435 VP instrument and a field-emission gun (FEG) equipped JEOL JSN6700F instrument. Elemental analyses of the films were performed by electron probe microanalysis (EPMA) using a CAMECA SX50 instrument. The films were submitted to X-ray photoelectron spectrometry (XPS) on an ESCALAB-MkII (VG Scientific) instrument. The photoelectron spectra were excited using non-monochromatized Mg Kα radiation ($h\nu$ = 1253.6 eV) with a total instrumental resolution of ±0.5 eV. Analyses were performed after etching of the film superficial layers with Ar ions. The room-temperature magnetic properties of the films were characterized using a Quantum Design MPMS2 superconducting quantum interference device magnetometer. The magnetic field was applied parallel to the film plane. The diamagnetic contribution from the substrate was negligibly small compared to the magnetization of the films.

Results

Characterization and thermal behavior of the precursors.— The mass spectra of the two compounds are characterized by the occurrence of relatively intense molecular peaks corresponding to the monomer $[FeL_2]^+$ and to the free ligand $[HL]^+$. There are no peaks at mass-to-charge (m/z) ratios higher than the value expected for FeL_2, i.e., 338 amu for compound 1 and 394 amu for compound 2. This was expected for compound 2, which is monomeric in the solid state.[20] Compound 1 is dimeric in the solid state,[20] so that additional studies such as vapor pressure measurement are needed to confirm the monomeric structure in the gas phase.

Figures 2 and 3 show the mass spectra ion peak intensity vs temperature for compounds 1 and 2, respectively. Before commenting, it is worth noting that the observed gaseous products did not depend on whether hydrogen had been added or not.

For compound 1 [Fig. 2, L = $(C_3H_7)NC(CH_3)N(C_3H_7)$], no major changes occur in the temperature range 110–160°C (not shown). Further temperature increase results in the decomposition of the compound and in the ensuing intensity decrease in the $[FeL_2]^+$ peak. At 250°C, the intensity is close to the background, indicating that the decomposition is maximal. The main gaseous compounds are the free ligand HL (m/z = 142), acetonitrile (m/z = 41), and $(CH_3)_2CHNH$ (m/z = 58).

Figure 3 shows the mass spectra ion peak intensity vs temperature for compound 2 [L = $(C_4H_9)NC(CH_3)N(C_4H_9)$] in the presence of hydrogen. Decomposition of compound 2 starts at 150°C as proved by a considerable decrease in the intensity of the initial compound ion peaks. Decomposition is maximal at 250°C. The main gaseous compounds are the free ligand HL (m/z = 170), CH_3CN (m/z = 41), C_4H_8 (m/z = 56), C_4H_9 (m/z = 57), and $(CH_3)_2CHNH$ (m/z = 58). The evolution of the intensity of the molecular peak is not sharp. This may be attributed to the relatively low vaporization stability of the compound. Similarly, the curves corresponding to $[HL]^+$, $[CH_3CN]^+$, and $[(CH_3)_2CHNH]^+$ have complex profiles because the ions originate both from the thermal decomposition of FeL_2 when the appropriate temperature is reached and from the fragmentation of FeL_2 and of some products (e.g., HL) under electron impact.

Elemental analysis of the films.— Table II shows the carbon and nitrogen contents of the films as determined by EPMA and the main

Table II. Carbon and nitrogen content and identified phases of the films, determined by EPMA and XRD, respectively (see text for sample code).

Code	$T_{deposition}$ (°C)	C (atom %)	N (atom %)	Identified phases	Possible additional phases
1A350	350	24	0	Fe_3C	Fe
1A400	400	28	0	Fe, Fe_3C, Fe_4C	—
1A450	450	33	0	Fe_3C, Fe_4C	Fe
2A280	280	18	0	Fe_4C	Fe, Fe_3C
2A300	300	18	0	Fe_4C	Fe, Fe_3C
2A320	320	15	7	Fe_3C, Fe_4N	Fe
2A350	350	17	7	Fe_3C, Fe_4N	Fe
2B280	280	12	9	Fe_4N	Fe, Fe_3C
2B300	300	19	7	Fe_3C, Fe_4N	Fe

Table III. Peak positions in GIXRD patterns of deposited films.

Code Presence of N (EPMA)	1A350 No	1A400 No	1A450 No	2A280 No	2A300 No	2A320 Yes	2A350 Yes	2B280 Yes	2B300 Yes
Components					2θ (°)				
$Fe_3C(121)$	37.80	37.76	37.80						
$Fe_3C(002)$	39.74	39.85	39.78				39.77		39.73
$Fe_3C(201)$	40.74	40.75	40.71						
$Fe_4C(111)$		41.48	41.48	41.49	41.44				
$Fe_4N(111)$						41.27	41.29	41.24	41.31
Cu(111): 43.40	43.43	43.41	43.42	43.45	43.40	43.41	43.42	43.41	43.45
α-Fe(110); $Fe_3C(220)$	44.69	44.73	44.62	44.76	44.70	44.62	44.69	44.67	44.69
$Fe_3C(112)$	45.86	45.93				45.95	45.92		45.89
$Fe_4C(200)$				48.25	48.11				
$Fe_4N(200)$						47.96	47.94	48.01	48.02
$Fe_3C(221)$	49.20	49.23	49.11						
Cu(200): 50.55	50.55	50.55	50.56	50.57	50.51	50.54	50.54	50.52	50.56
$Fe_3C(301)$	58.14	58.10	58.08						
α-Fe(200)		65.06							
$Fe_4N(220)$						70.20	70.12	70.10	70.21
Cu(220): 74.29	74.22	74.21	74.29	74.26	74.23	74.22	74.22	74.21	74.22
$Fe_3C(401)$	78.23								
α-Fe(211)	82.95(wide)	82.40							

phases identified by GIXRD (see next paragraph). In this and the following tables, sample code shows the precursor (1 or 2), the reactor (A or B), and the temperature of deposition in degrees Celsius. The average thickness of films was approximately 250–300 nm. The oxygen content was below the EPMA detection limit. XPS was performed on as-processed films. From the decomposition of XPS Fe 2p and C 1s peaks and from literature data for iron-containing films,[30] the films contained iron oxide (Fe $2p_{3/2}$ at ~712 eV) and graphitic and organic carbon as minority components. Iron oxides are considered as surface contaminants because they were most probably formed when the samples were exposed to ambient atmosphere. Depth profile analyses revealed uniform composition in the films (to the extent of the zones sputtered with low energy Ar ions) except surface contaminants. From GIXRD and XPS (vide infra), the main iron-based deposited species are iron carbides (Fe_3C, Fe_4C), iron nitride Fe_4N, and metallic iron. Table II shows that nitrogen was detected in four films grown from precursor 2 at low H/P ratio at 320 and 350°C, and at high H/P ratio at 280 and 300°C.

XRD.— GIXRD patterns for films prepared from compounds 1 and 2 are presented in Fig. 4 and 5, respectively. Table III is a synoptic of the 2θ angles calculated for copper (a = 3.6078 Å, F-type lattice) and measured on the X-ray patterns up to 80°. There is a strong fit between the calculated and observed 2θ values for the diffraction lines (111), (200), and (220) from the copper substrate, and this allows using it as an internal 2θ standard. Neither iron nor copper oxides were detected. The patterns contain lines attributable to α-Fe (JCPDS file no. 6-696) and Fe_3C (JCPDS file no. 34-1). They also contain lines attributable to Fe_4C or Fe_4N depending on the sample. Fe_4C has two allotropic forms.[3,31,32] The observed form is isostructural with γ′-Fe_4N (JCPDS file no. 6-0627): primitive

Table IV. Decomposition of the Fe $2p_{3/2}$ and C 1s XPS peaks of films prepared from compound 2: BE and energy drifts are in eV. Energy drifts are measured from peak Fe1 for Fe peaks and peak C2 for C peaks.

Peak code	Fe1═Fe + Fe nitrides $2p_{3/2}$ BE atom % $Fe1/Fe_{total}$	Fe2═Fe carbides $2p_{3/2}$ BE (E drift) atom % $Fe2/Fe_{total}$	Fe3═Fe oxides $2p_{3/2}$ BE (E drift) atom % $Fe3/Fe_{total}$	C1═C carbides 1s BE (E drift) atom % $C1/C_{total}$	C2 = graphitic C 1s BE atom % $C2/C_{total}$	C3 = organic C 1s BE (E drift) atom % $C3/C_{total}$
Sample						
2A260	706.6	708.3 (1.7)	710.6 (4.0)	—	—	—
	46	32	22			
2A280	706.5	708.3 (1.8)	710.7 (4.2)	282.5 (−1.5)	284.0	285.9 (1.9)
	43	38	19	50	36	14
2A300	706.6	708.3 (1.7)	710.8 (4.2)	283.1 (−1.9)	285.0	287.6 (2.6)
	42	45	13	71	17	12
2A320	707.6	709.3 (1.7)	711.2 (3.6)	283.9 (−1.9)	285.8	289.1 (3.3)
	43	32	25	52	32	16
2A350	707.7	709.6 (1.9)	711.7 (4.0)	283.3 (−1.4)	284.7	No peak
	36	39	25	37	63	

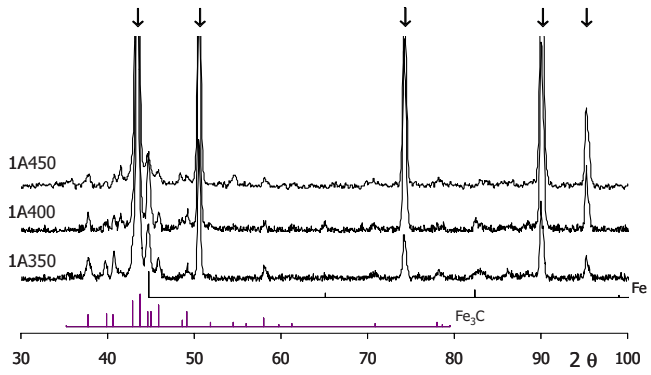

Figure 4. (Color online) XRD analysis of the films deposited from compound 1 on copper (↓) substrates.

cubic lattice, with a = 3.790 Å for Fe_4N [33] and a = 3.678 Å for Fe_4C.[3,31] There is no recorded X-ray diffraction (XRD) pattern for Fe_4C in the JCPDS database. The calculated Fe_4C diffraction pattern can be deduced from Fe_4N by considering the difference in the cell constant. Using the copper substrate as an internal 2θ standard, the lines at 41.25 ± 0.02 and 47.99 ± 0.02° were indexed as Fe_4N(111) and Fe_4N(200) reflections and those observed at 41.45 ± 0.02 and 48.19 ± 0.04° as Fe_4C(111) and Fe_4C(200) reflections (Table III). The systematic discrepancy of 0.2° between corresponding diffraction angles is significantly larger than the differences between the calculated and observed copper angles (0.05° at most). Therefore, the distinction between Fe_4C and Fe_4N becomes unambiguous.

There is an ambiguity in the determination of metallic iron because the α-Fe strongest reflection (110) at 44.67° and Fe_3C strong reflection (220) at 44.59° almost overlap. Therefore, the reflection observed at ca. 44.6–44.7° in every pattern can be attributed to either Fe and Fe_3C. Moreover, the Fe_3C strongest reflections at 43.77 and 42.90° may be hidden by the Cu(111) reflection at 43.40°.

From the GIXRD patterns shown in Fig. 4 and the data extracted from them and analyzed in Table III, the films processed from compound 1 systematically contain Fe_3C. For the film deposited at 400°C (1A400), two weak reflections at 2θ = 65.06 and 82.40° can be attributed to α-Fe(200) and α-Fe(211), respectively. For the film deposited at 350°C (1A350), reflection (200) does not show, and reflection (211) may be included in the wide reflections observed at 82.95°. For the film deposited at 450°C (1A450), there is no iron reflection except for the one that is also attributable to Fe_3C. Finally, for the films deposited at 400 and 450°C, there is a reflection at 41.48° that matches the Fe_4C strongest reflection (111).

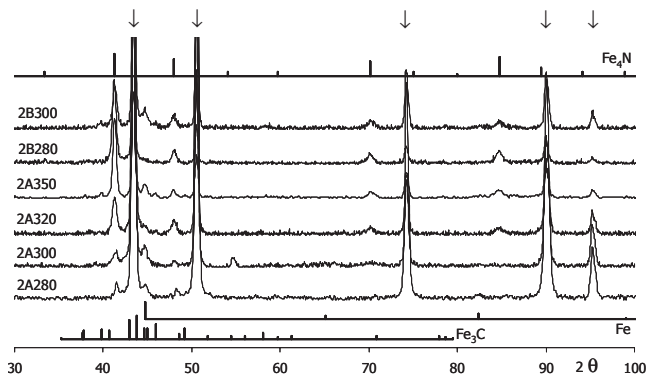

Figure 5. XRD analysis of the films deposited from compound 2 on copper (↓) substrates.

Despite the narrow temperature range investigated, the films deposited from compound 2 present noticeable differences (Fig. 5, Table III). The possible presence of metallic iron can only be deduced from the line ca. 44.7°, which may also belong to Fe_3C. Lines at 39.7 and 45.9° indicate the presence of Fe_3C in the films prepared at 320 and 350°C at low H/P, and at 300°C at high H/P ratio. The patterns of the films prepared at 280 and 300°C at low H/P ratio show lines from Fe_4C, while the other four patterns for the films prepared both at high and low H/P ratios show lines from Fe_4N. From the intensity of reflection (111), Fe_4N appears as the main component and is markedly (111)-oriented. The films showing the X-ray pattern of Fe_4N are those in which nitrogen was evidenced by EPMA (Table II).

The weak intensity of most reflections and the overlap among some of them preclude any attempt to use the XRD patterns to quantitatively or even semiquantitatively analyze the three-phase mixture in the films.

XPS analysis.— Table IV shows the decomposition of Fe $2p_{3/2}$ peaks for five films prepared from compound 2 at low H/P values in the temperature range 260–350°C. The Fe peak was decomposed into four peaks. The first one (Fe1) at ca. 707–708 eV is attributed to metallic iron and Fe_4N because it has been reported that the Fe $2p_{3/2}$ binding energy (BE) in iron nitrides is too close to that of the metal to be used to distinguish a nitride from α-Fe.[34] This point has been confirmed from the XPS analyses of amorphous γ′-Fe_4N thin films by Fehlner et al.[35] and from the investigation of the electronic structure of ultrathin γ′-Fe_4N(100) films by Navio et al.[36,37] The second peak (Fe2) at ca. 708–709 eV was attributed to the carbides Fe_nC (n = 3, 4). The other two peaks at ca. 710–712 and 713–714 eV were attributed to iron oxides (Fe3) and to the shake-up satellite, respectively. The C 1s peak was decomposed in three peaks (Table IV), namely carbides (C1), graphitic carbon (C2), and other, e.g., organic carbon (C3).

The atomic ratios $Fe1/Fe_{total}$, $Fe2/Fe_{total}$, $Fe3/Fe_{total}$, $C1/C_{total}$, $C2/C_{total}$, and $C3/C_{total}$, where Fe_{total} and C_{total} stand for total iron and carbon contents, respectively, were deduced from their respective peak surface areas. They are reported in Table IV. The surface-generated iron oxide covers the other iron species. Therefore, the percentage of iron oxides ($Fe3/Fe_{total}$) is most likely overestimated with regard to other iron species ($Fe1/Fe_{total}$ and $Fe2/Fe_{total}$) due to the relatively weak information depth of XPS.

From the XRD, the films deposited at 260, 280, and 300°C do not contain Fe_4N. The peak observed at ca. 707.0 eV ascertains the presence of metallic iron. The ratio $Fe2/Fe_{total}$ increases with deposition temperature. The films deposited at 320 and 350°C do contain Fe_4N from the XRD. The presence of nitrogen in as-deposited films was proved by EPMA (Table II). However, no N 1s XPS peak was observed, probably because Fe_4N was decomposed upon etching the surface of the films. The XPS peak at ca.707 eV may thus be attributed to metallic iron present before the etching and to metallic iron formed upon etching. Table IV shows that the formation of Fe_4N at 320°C is marked by the decrease in the atomic ratios $Fe2/Fe_{total}$ and $C1/C_{total}$ from 0.45 to 0.32 and from 0.71 to 0.52, respectively.

Film morphology.— The films deposited on well-polished copper present a gray, mirrorlike metallic surface. This morphology is more pronounced for the films processed from precursor 2. Figure 6 shows surface SEM micrographs of the films deposited from precursor 1, at 350°C (Fig. 6a) and at 400°C (Fig. 6b). Figure 7 shows the micrographs for the films deposited from precursor 2, at 280°C (Fig. 7a) and at 350°C (Fig. 7b). When deposited at a temperature below 300°C, the films are made of densely packed nanocrystallites (size < 100 nm), independently of the precursor. This nanostructure results in films with a remarkably smooth surface. A comparison between the films deposited at 350°C from precursors 1 and 2 (Fig. 6a and 7b, respectively) reveals different microstructures. The film deposited from precursor 1 shows poorer crystallinity than the one deposited from precursor 2. The former mainly contains Fe_3C,

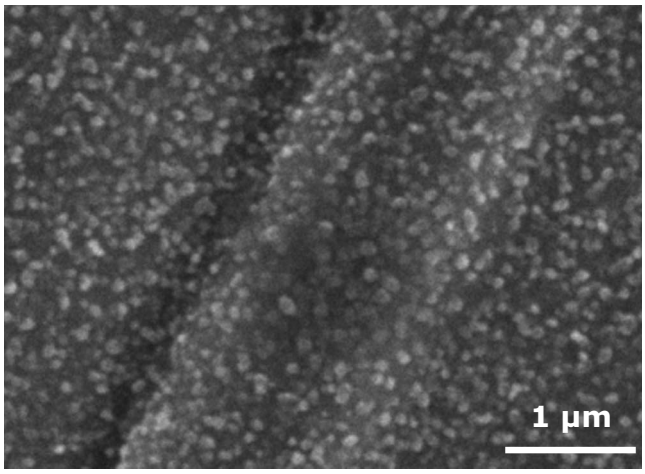

(a)

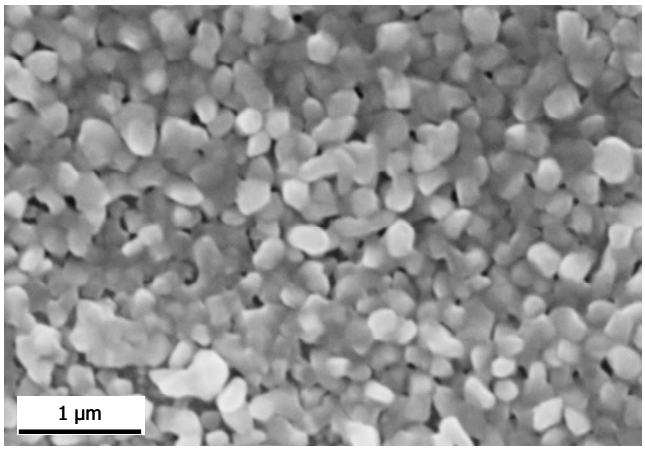

(b)

Figure 6. SEM-FEG surface micrographs of films deposited from compound 1 at (a) 350 and (b) 400°C.

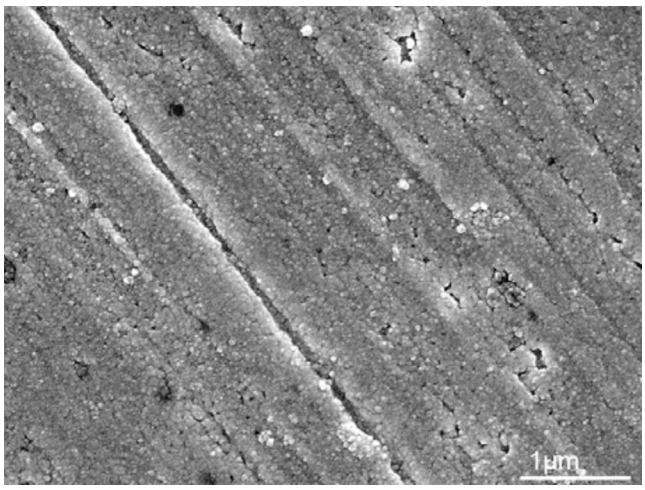

(a)

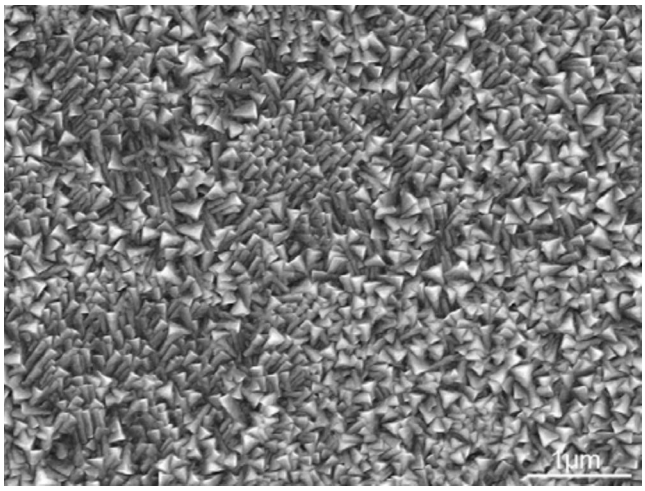

(b)

Figure 7. SEM-FEG surface micrographs of films deposited from compound 2 at (a) 280 and (b) 350°C.

while the film prepared from precursor 2 at 350°C (Fig. 7b) is well crystallized and shows the ⟨111⟩ texture of Fe_4N evidenced by the XRD pattern (Fig. 5). The use of different deposition temperatures and of two precursors results in striking differences among the microstructures of the processed films. This observation is correlated with the change in the composition of the films as discussed below.

Magnetic properties.— Figure 8 shows $4\pi M$-H loops for the 1A400 and 2A320 films. For the 1A400 film which contains Fe_3C and α-Fe as a presumably additional phase, saturation magnetization ($4\pi M_s$ = 4.1 kG) and coercive field (H_c = 180 Oe) values are similar to those recently reported for Fe_3C/α-Fe powders obtained by reaction milling.[38] The magnetization curve recorded for the ⟨111⟩-textured γ′-Fe_4N film (2A320) exhibits a saturation magnetization of $4\pi M_s$ = 13.6 kG and a coercive field of H_c = 130 Oe. The saturation magnetization value is lower than that of the bulk value for pure γ′-Fe_4N (18–21 kG).[39] This difference may be attributed to size effects, because at room temperature, the $4\pi M_s$ drops with particle size.[40] It may also be due to the presence of free carbon in the film. The decrease in the saturation magnetization due to the presence of free carbon has already been demonstrated for the MOCVD processed Ni films.[41] The presently reported H_c value (130 Oe) is much higher than that for the γ′-Fe_4N(001)-oriented films grown on MgO(001) or MgO(111) substrates (in the 35–45 Oe range).[42] This difference can be assigned to the morphology of the films. Oriented films on MgO(001) or MgO(111) exhibit large grains in which spins are easily arranged. The MOCVD processed films containing γ′-Fe_4N exhibit small crystallites for which domain walls are probably harder to move.

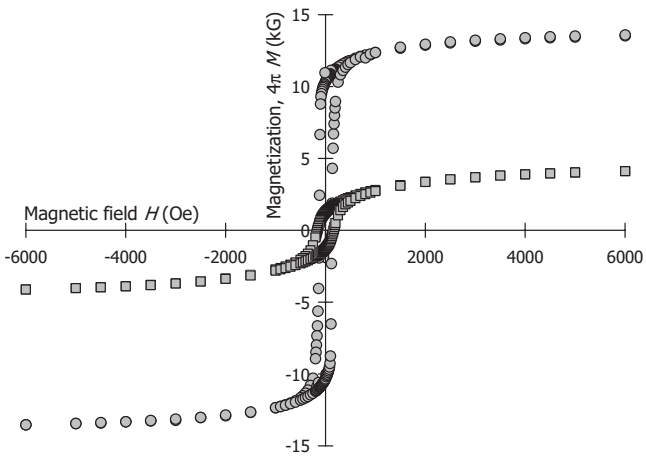

Figure 8. Magnetization ($4\pi M$) and magnetic field (H) loops of films 1A400 (squares) and 2A320 (circles).

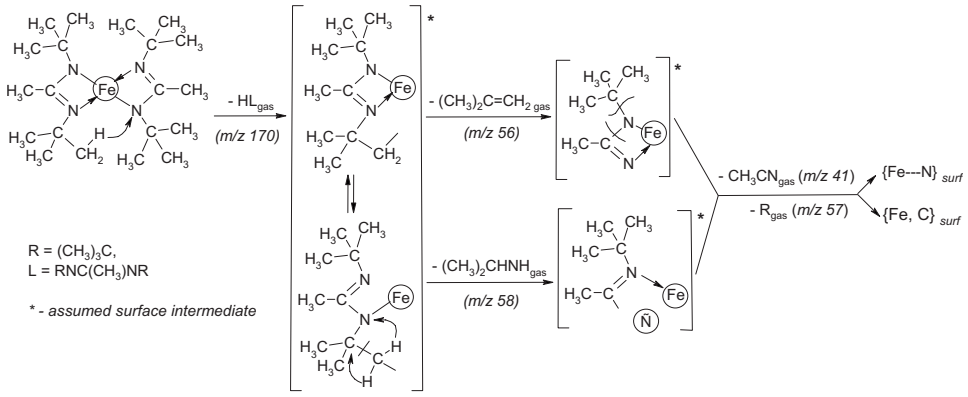

Figure 9. Proposed decomposition scheme on the growing surface for precursor 2.

Discussion

The films deposited from compound 2 contain less carbon-containing species than those processed from compound 1. Moreover, compound 2 gives a lower onset deposition temperature and higher growth rate (detailed results on growth rates from the two precursors were published in Ref. 43). For these reasons, Fe(^{t}Bu-MeAMD)$_2$ appears as a more interesting precursor for Fe-containing films than Fe$_2$(^{i}Pr-MeAMD)$_4$. The affinity of Fe to C is responsible for the formation of Fe_3C in most investigated conditions. There exist, however, processing conditions for which either metallic Fe or Fe_4N and Fe_4C are also formed. Fe_4N and Fe_4C are isostructural compounds. Their crystal structure is a primitive cubic lattice with four Fe atoms and one N (C) atom per cell, in a semi-antiperovskite-type structure ($FeXFe_3$ with X = N or C). The unit cell constants differ by ca. 3% only. Therefore, their identification by means of XRD is not straightforward. In this study, the use of X-ray reflections from the copper substrate as Bragg angles internal standard removed this difficulty.

This is a report on CVD of Fe_4C while, as mentioned in the Introduction, there are but a few papers on CVD of Fe_4N. Both Funakubo et al.[27] and Takahashi et al.[26] operated at high temperature and atmospheric pressure conditions with complex gas phases involving separate precursors for Fe and N. The process reported in the present work operates in significantly simpler conditions.

The formation of Fe_4N in the film is compatible with the analysis of the mass spectrometric data on gas-phase composition upon thermal decomposition of compound 2. Based on these data, Fig. 9 resumes the following mechanism which is proposed for the decomposition of compound 2 (all conversions take place on the surface): (*i*) migration of H from one ligand to another, dissociation of the Fe–N bond, and release of free ligand HL into the gas phase; (*ii*) decomposition of remaining [Fe(L–H)] with (a) release of the radical $HNCH(CH_3)_2$ (m/z = 58) in the gas phase, formation of carbon and of the surface intermediate [Fe–C(CH_3) = NR], and (b) release of methylpropene $(CH_3)_2C{=}CH_3$ (m/z = 56) in the gas-phase and formation of the surface intermediate [Fe–N=C(CH_3)NR]; and (*iii*) decomposition of the surface intermediates with the release of acetonitrile CH_3CN (m/z = 41) and *tert*-butyl radical R (m/z = 57) and formation of (a) Fe–N and (b) Fe and C on the surface. Migration of H from one ligand to another after chelate-ring opening is the typical process for metal–chelate complexes with organic ligands.[28] The formation of organic products with an m/z lower than for the ligand indicates that a pure reduction of the compound by hydrogen does not take place. This is also supported by recent literature data on the decomposition of copper amidinates on Ni surface under high vacuum conditions.[44]

Conclusion

This reported study of iron amidinates tentatively used as precursors for the MOCVD of iron and iron nitrides. Iron amidinates were chosen because they contain no oxygen atoms and no Fe–C bonds. Between the two alkylacetamidinates retained, the (1) isopropyl derivative is dinuclear in the solid state and the (2) *tert*-butyl derivative is mononuclear. Mass spectrometry showed them to be mononuclear in the gas phase. Compound 1 proved to provide more carbon-based species than compound 2.

Fe and Fe_3C were present in the films. The films also contained either Fe_4C or Fe_4N depending on the temperature and the hydrogen to precursor concentrations in the input gas.

This work may be considered as a screening approach for the use of iron amidinates as precursors for preparing iron-based materials by MOCVD. The determination of the appropriate processing window for the deposition of either metallic Fe or Fe_4N, or even iron carbides, requires further investigation of the influence of reactive atmospheres, of surface chemistry, and possibly of appropriate post-deposition treatments. More precisely, a prerequisite for the stabilization of pure Fe should be good venting conditions at the growing surface. Such conditions are ultimately illustrated by the ALD process and should involve a reducing gas such as hydrogen, preferably in the atomic state.

Acknowledgments

We are indebted to Yannick Thébault and Djar Oquab, Institut National Polytechnique, Toulouse for the SEM studies, and to Sophie Gouy and Philippe de Parseval, Observatoire Midi-Pyrénées, Toulouse for the EPMA analyses. This work was supported by the EC under contract no. NMP3-CT-2005-500140 and no. MC-IIF-39728, by the French Agence Nationale de la Recherche (ANR) under contract no. NT05-3_41834, and by CNRS through a grant awarded to V.K.

Nikolaev Institute of Inorganic Chemistry SB RAS assisted in meeting the publication costs of this article.

References

1. F. Senocq, F. D. Duminica, F. Maury, T. Delsol, and C. Vahlas, *J. Electrochem. Soc.*, **153**, G1025 (2006).
2. S. I. Roberson, D. Finello, A. D. Banks, and R. F. Davis, *Thin Solid Films*, **326**, 47 (1998).
3. M. Deng, C.-F. Huo, L.-L. Bao, X.-R. Shi, Y.-W. Li, J. Wang, and H. Jiao, *Chem. Phys. Lett.*, **448**, 83 (2007).
4. M. L. Hitchman and K. F. Jensen, *Chemical Vapor Deposition: Principles and Applications*, Academic, London (1993).
5. J. M. Dubois, *Useful Quasicrystals*, World Scientific, River Edge, NJ (2005).
6. U. Patil, R. Thomas, A. Milanov, R. Bhakta, P. Ehrhart, R. Waser, R. Becker, H.-W. Becker, M. Winter, K. Merz, et al., *Chem. Vap. Deposition*, **12**, 172 (2006).
7. R. Thomas, P. Ehrhart, M. Roeckerath, S. van Elshocht, E. Rije, M. Luysberg, M. Boese, J. Schubert, M. Caymax, and R. Waser, *J. Electrochem. Soc.*, **154**, G147 (2007).
8. G. J. M. Dormans, *J. Cryst. Growth*, **108**, 806 (1991).
9. G. T. Stauf, D. C. Driscoll, P. A. Dowben, S. Barfuss, and M. Grade, *Thin Solid Films*, **153**, 421 (1987).
10. H. J. Haugan, B. D. McCombe, and P. G. Mattocks, *J. Magn. Magn. Mater.*, **247**, 296 (2002).
11. P. A. Lane and P. J. Wright, *J. Cryst. Growth*, **204**, 298 (1999).
12. P. A. Lane, P. J. Wright, P. E. Oliver, C. L. Reeves, A. D. Pitt, and J. M. Keen,

Chem. Vap. Deposition, **3**, 97 (1997).
13. P. J. Walsh and N. Bottka, *J. Electrochem. Soc.*, **131**, 444 (1984).
14. R. Kaplan and N. Bottka, *Appl. Phys. Lett.*, **41**, 972 (1982).
15. R. Feurer, M. Larhrafi, R. Morancho, and R. Calsou, *Thin Solid Films*, **167**, 195 (1988).
16. W. Luithardt and C. Benndorf, *Thin Solid Films*, **290–291**, 200 (1996).
17. K. Michkova, A. Schneider, H. Gerhard, N. Popovska, I. Jipa, M. Hofmann, and U. Zenneck, *Appl. Catal., A*, **315**, 83 (2006).
18. D. V. Baxter, M. H. Chisholm, G. J. Gama, A. L. Hector, and I. P. Parking, *Chem. Vap. Deposition*, **1**, 49 (1995).
19. S. Park, S. Lim, and H. Choi, *Chem. Mater.*, **18**, 5150 (2006).
20. B. S. Lim, A. Rahtu, J.-S. Park, and R. G. Gordon, *Inorg. Chem.*, **42**, 7951 (2003).
21. B. S. Lim, A. Rahtu, and R. Gordon, *Nat. Mater.*, **2**, 749 (2003).
22. V. Krisuyk, L. Aloui, N. Prud'homme, B. Sarapata, F. Senocq, D. Samélor and C. Vahlas, *ECS Trans.*, **25**(8), 581 (2009).
23. D. Ecija, E. Jimenez, J. Camarero, J. M. Gallego, J. Vogel, N. Mikuszeit, N. Sacristan, and R. Miranda, *J. Magn. Magn. Mater.*, **316**, 321 (2007).
24. L. L. Wang, W. T. Wang, W. T. Zheng, N. Ma, H. B. Li, Q. F. Guan, D. H. Jin, and Z. G. Zong, *J. Alloys Compd.*, **443**, 43 (2007).
25. T. Takahashi, N. Takahashi, T. Nakamura, T. Kato, K. Furukawa, M. G. Smith, and C. P. Riedi, *Solid State Sci.*, **6**, 97 (2004).
26. T. Takahashi, N. Takahashi, N. Tamura, T. Nakamura, M. Yoshioda, W. Inami, and Y. Kawata, *J. Mater. Chem.*, **11**, 3154 (2001).
27. M. Funakubo, N. Kieda, M. Kato, and N. Mizutani, *J. Mater. Sci.*, **25**, 5303 (1990).
28. A. E. Turgambaeva, V. V. Krisyuk, P. A. Stabnikov, and I. K. Igumenov, *J. Organomet. Chem.*, **692**, 5001 (2007).
29. T. C. Xenidou, A. G. Boudouvis, N. C. Markatos, D. Samélor, F. Senocq, A. N. Gleizes, N. Prud'homme, and C. Vahlas, *Surf. Coat. Technol.*, **201**, 8868 (2007).
30. C. D. Wagner, A. V. Naumkin, A. Kraut-Vass, J. W. Allison, C. J. Powell and J. R. Rumble, Jr., NIST X-ray Photoelectron Spectroscopy Database, NIST Standard Reference Database 20, Version 3.5 (2003).
31. L. Peltzer y Biancá, J. Desimoni, and N. E. Christensen, *Physica B*, **354**, 341 (2004).
32. P. Villars, L. D. Calvert, and W. B. Pearson, *Pearson's Handbook of Crystallographic Data for Intermetallic Phases*, ASM International, Materials Park, OH (1991).
33. H. Jacobs, D. Rechenbach, and U. Zachwieja, *J. Alloys Compd.*, **227**, 10 (1995).
34. D. C. Kothari, M. R. Nair, A. A. Rangwala, K. B. Lal, P. D. Parbhawalkar, and P. M. Hole, *Nucl. Instrum. Methods Phys. Res. B*, **7–8**, 235 (1985).
35. T. P. Fehlner, M. M. Amini, W. F. Stickle, O. A. Pringle, G. J. Long, and F. P. Fehlner, *Chem. Mater.*, **2**, 263 (1990).
36. C. Navio, J. Alvarez, M. J. Capitan, F. Yndurain, and R. Miranda, *Phys. Rev. B*, **78**, 155417 (2008).
37. C. Navio, J. Alvarez, M. J. Capitan, D. Ecija, J. M. Gallejo, F. Yndurain, and R. Miranda, *Phys. Rev. B*, **75**, 125422 (2007).
38. D. Chaira, B. K. Mishra, and S. Sangal, *J. Alloys Compd.*, **474**, 396 (2009).
39. H. Naganuma, R. Nakatani, Y. Endo, Y. Kawamura, and M. Yamamoto, *Sci. Technol. Adv. Mater.*, **5**, 101 (2004).
40. W. H. Zhong, B. K. Tay, S. P. Lau, X. W. Sun, S. Li, and C. Q. Sun, *Thin Solid Films*, **478**, 61 (2005).
41. L. Brissonneau, D. deCaro, D. Boursier, R. Madar, and C. Vahlas, *Chem. Vap. Deposition*, **5**, 143 (1999).
42. K. Higashi and K. Oda, *Trans. Mater. Res. Soc. Jpn.*, **29**, 3103 (2004).
43. A. N. Gleizes, V. V. Krisyuk, L. Aloui, A. E. Turgambaeva, B. Sarapata N. Prud'Homme, F. Senocq, D. Samélor, A. Zielinska-Lipiec, F. Dumestre, et al., *ECS Trans.*, **25**(8), 181 (2009).
44. Q. Ma, H. Guo, R. Gordon, and F. Zaera, *Chem. Mater.*, **22**, 352 (2010).